

A Coarse-to-fine Robotic Fabric Alignment System Integrating Visual Servoing and Admittance Control

Jiaming Qi, Peng Zhou, Lei Yang, Liang Lu, Yan Ding, Pai Zheng, *Senior Member, IEEE*, David Navarro-Alarcon, *Senior Member, IEEE* and Jia Pan, *Senior Member, IEEE*

Abstract—Fabric alignment is essential to key production processes such as cutting, sewing, and fusing in garment manufacturing. Traditionally, this task has relied heavily on the dexterity and expertise of skilled human workers. Although automated systems have been introduced, they often lack the flexibility required for complex alignment tasks. In this paper, we present a novel robotic fabric alignment framework that fully automates the process with high precision and adaptability. First, we propose a coarse-to-fine alignment strategy, where an initial imprecise target position is roughly computed based on a basic perception module and eye-to-hand calibration. This is followed by a sliding mode control (SMC)-based visual servoing approach (in an eye-on-hand configuration) to ensure a close-up view of feedback features for the fine alignment process. Additionally, we consider system disturbances estimated by a fuzzy logic system (FLS) and combine it with the controller to further enhance the system’s robustness. Finally, we developed an advanced end-effector equipped with force/torque (F/T) sensors and air-powered needle grippers for gentle fabric manipulation using admittance control. We validate our framework through a series of experiments that demonstrate its effectiveness in fabric alignment tasks.

Note to Practitioners—Fabric alignment in garment production is a labor-intensive task that heavily relies on skilled human workers. Existing automated fabric alignment machines are typically limited to specific fabric shapes, patterns, and materials. Furthermore, transitioning between different fabric types requires extensive testing and adjustments, resulting in a lack of adaptability and flexibility. In this work, we propose a robotic fabric alignment system based on a coarse-to-fine alignment strategy. The initial target pose is roughly estimated using a basic perception module and eye-to-hand calibration, followed by fine adjustments through a visual servoing controller in an eye-on-hand configuration. Additionally, to ensure gentle handling, the contact force between the end-effector and the platform surface is optimized using admittance control. The proposed system offers practitioners a comprehensive solution for automating fabric alignment with high precision, while maintaining flexibility and adaptability across various fabric types and initial environmental conditions.

Index Terms—Automation; Fabric manipulation; Visual servoing; Admittance control.

I. INTRODUCTION

Robotic automation has transformed numerous industrial processes, significantly enhancing efficiency and precision

This work is supported in part by the Innovation and Technology Commission of the HKSAR Government under the InnoHK initiative and in part by the National Natural Science Foundation (NSFC) of China under 62403211. Corresponding author: Peng Zhou and Jia Pan

J. Qi, P. Zhou, L. Yang and J. Pan are with the Department of Computer Science, The University of Hong Kong, Pok Fu Lam, Hong Kong.

Y. Ding is with the Shanghai Artificial Intelligence Laboratory.

P. Zheng and D. Navarro-Alarcon are with The Hong Kong Polytechnic University, Kowloon, Hong Kong.



Fig. 1. Fabric alignment is a fundamental task essential to various garment manufacturing processes, including (from left to right) fabric cutting, sewing, fusing, and pattern matching.

across various industries and manufacturing sectors [1]. However, garment manufacturing presents unique challenges that set it apart from other automated industries [2]. Unlike sectors such as automotive assembly or electronics manufacturing, where robots predominantly handle rigid components, garment manufacturing involves the manipulation of highly deformable materials [3]–[5] like fabrics.

Fabrics are deformable objects that easily change shape when subjected to external forces. However, fabric manipulation is integral across all stages of the garment production process. Among all the production processes, fabric alignment is a critical operation in garment manufacturing, serving as the foundation for key processes such as cutting, sewing, and fusing (see Fig. 1). The precision of fabric alignment directly affects the quality and efficiency of these processes, making it essential for achieving consistent, high-quality production. Traditionally, fabric alignment has been performed manually, relying on the dexterity and experience of skilled workers to ensure accuracy. While automated systems have been introduced to streamline production, they are often rigid and struggle to adapt to the inherent variability of fabrics, such as changes in texture, elasticity, and shape. These limitations pose significant challenges, particularly in an industry that requires flexibility to accommodate frequent shifts in fashion trends and production demands. As a result, there is a growing need for more advanced automation solutions that can handle the complexity of fabric alignment with greater precision and adaptability.

To develop a robotic system that meets the requirements, we conducted a detailed analysis of expert human workers performing fabric alignment and identified key practices that ensure high precision. Drawing on these insights, we integrated two air-powered needle grippers and designed a specialized robotic end-effector capable of securely grasping both ends of the fabric. This design minimizes deformation during fabric handling, thereby improving both alignment accuracy and operational efficiency. We also proposed a coarse-to-fine alignment strategy, beginning with an initial rough computation of the target alignment position using a basic perception module and eye-to-hand calibration. This is followed by a sliding mode

control (SMC)-based visual servoing approach (in an eye-on-hand configuration) to provide close-up feedback for the fine alignment process, mimicking the detailed visual feedback techniques used by skilled workers during fabric alignment.

To further enhance the system's robustness, we incorporated a fuzzy logic system (FLS)-based approach to estimate system disturbances, which is integrated into the controller design. Additionally, admittance control was implemented to enable robust yet delicate grasping and placement of fabrics in various configurations, ensuring stable and gentle handling of fabrics with diverse properties. We validated our framework through a series of experiments that demonstrated its effectiveness in fabric alignment tasks. A video of the experiments can be downloaded from <https://github.com/JiamingQi-Tom/PaperVideos/raw/refs/heads/master/paper5/video.mp4>

The contributions of this paper are summarized as follows:

- We leverage a coarse-to-fine alignment strategy to propose a novel robotic fabric alignment system with high precision and adaptability.
- We propose a new sliding modes control (SMC)-based visual servoing controller that utilizes a fuzzy logic system (FLS) to estimate disturbances, and thus, provides adaptiveness and robustness.
- We develop an advanced end-effector equipped with force/torque (F/T) sensors and air-powered needle grippers for gentle fabric manipulation using admittance control.

The rest of this article is organized as follows. In Section II, we carefully discuss the advantages and limitations of current mainstream approaches for fabric manipulation. The problem formulation is discussed in Section III. In Section IV, we provide a brief overview of admittance control in this paper. Fabric identification approach is presented in Section V. Details of the visual servoing-based fabric alignment control design and stability analysis are presented in Section VI. Experimental results are shown in Section VII. Section VIII presents concluding remarks and future work.

II. RELATED WORK

This section reviews the literature on deformable object manipulation (DOM) [6], focusing specifically on fabric manipulation and object alignment. It highlights the progression from traditional methods to more advanced, adaptive strategies.

A. Traditional Fabric Manipulation Techniques

In garment manufacturing, the majority of processes are still performed manually, with only a small portion of specific tasks being fully automated. Traditional approaches to fabric manipulation automation often rely on mechanical solutions, which are typically task-specific and lack the flexibility required to handle the variability and complexity of fabrics. For example, [7] introduces a versatile gripper capable of executing a wide range of grasps, simplifying tasks such as picking up folded garments or folding fabric in mid-air. Similarly, [8] designs an innovative robotic gripper inspired by human grasping strategies for handling fabric materials. Building on this, [9] proposes automation technologies for common manufacturing processes in garment factories. Despite these advancements,

traditional systems rely heavily on rigid-contact approaches for fabric manipulation. This reliance limits their adaptability and precision, particularly when dealing with fabrics of varying characteristics or operating in unstructured environments.

B. Visual Servoing and Admittance Control

Advancements in computer vision have made visual servoing a significant breakthrough in fabric manipulation [10]. In [11], system feedback is used to train a pseudo-kinematic model, which is then applied to folding and sorting tasks. The authors further extend their research to various manipulation tasks, demonstrating improved system stability and precision compared to purely mechanical methods [12]. Similarly, [13] introduces a model-based closed-loop control framework to enable human-robot collaboration for cooperative fabric manipulation. [14] presents a collaborative object transportation approach, enhancing the accuracy of deformation detection through data-driven depth estimation. Additionally, a grasping framework is proposed in [15] to support diverse grasping strategies for hybrid grippers. These studies showcase advanced manipulation techniques for robots and grippers, primarily relying on vision-based closed-loop feedback systems. However, these methods often require multiple iterative manipulations to determine optimal robot actions, making them less suitable for industrial applications where speed and efficiency are crucial.

Admittance control, on the other hand, enables robot-environment interaction by adjusting the robot's movements based on force feedback [16]. For example, [17] proposes a physical human-robot interaction approach using a robotic exoskeleton to address unknown dynamic characteristics. Subsequently, [18] develops an admittance-based controller for co-ordinated operations within constrained task spaces, preventing collisions with the environment. Combining admittance control with visual servoing offers a robust solution for managing the unpredictable dynamics of fabric manipulation, making it particularly advantageous in tasks requiring adaptability and precision.

C. Comparisons with Existing Systems

Existing fabric alignment techniques often struggle to adapt to the diverse and unstructured conditions encountered in real-world scenarios, making precise and reliable alignment difficult to achieve. Many approaches fail to adequately address the complexities introduced by uncertainties in fabric properties, environmental factors, and robot-fabric interactions, leading to compromised alignment accuracy and performance. Additionally, there is a notable research gap in the comprehensive integration of visual servoing, force control, and compensation mechanisms to enhance precision and robustness under varying environmental conditions.

This research introduces an innovative integrated control framework that combines visual servoing with admittance control, augmented by a Fuzzy Logic System-based compensation mechanism. The framework adopts a holistic approach to fabric alignment by accounting for both force interactions and variable initial environmental conditions. By unifying diverse control strategies, the proposed framework achieves superior

alignment performance, as validated through experimental results. Beyond fabric alignment, this approach shows potential for extending to other tasks, such as pick-and-place operations, that require high precision and dexterity. This versatility makes it a promising solution for robotic applications across various manufacturing sectors. By addressing existing limitations and contributing novel solutions, this research aims to advance the field of fabric alignment, paving the way for more robust and adaptable robotic automation systems in manufacturing.

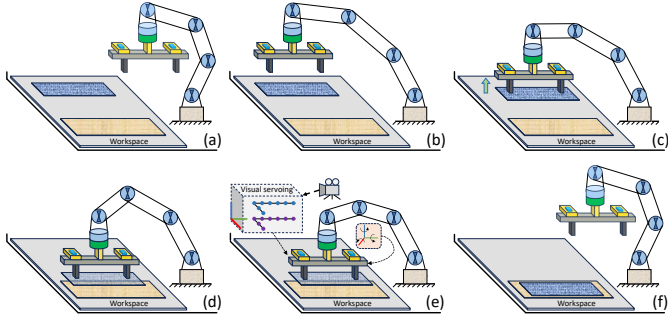


Fig. 2. Fabric alignment. (a) The G-fabric and A-fabric are initially placed randomly on the workspace. (b) The robot moves above the G-fabric. (c) The robot grasps the G-fabric and lifts it up. (d) The robot moves the G-fabric above the A-fabric while maintaining a certain distance (initial alignment). (e) The robot starts the visual servoing-based alignment. (f) The G-fabric and A-fabric are aligned according to the requirements.

III. SYSTEM OVERVIEW

Notation: A vector and a matrix are denoted by lowercase and uppercase bold letters, respectively, e.g., \mathbf{v} and \mathbf{M} . $\mathcal{F}_x \mathbf{p}$ represents a point \mathbf{p} within the frame \mathcal{F}_x . By default, all points are defined in the world frame \mathcal{F}_w . $\mathcal{F}^a \mathbf{T}_{\mathcal{F}_b} \in SE(3)$ denotes the transformation from frame \mathcal{F}_a to frame \mathcal{F}_b .

The schematic illustration of the designed fabric alignment framework is shown in Fig. 2. The proposed framework is designed to address challenges in textile, garment manufacturing, and other fabric processing industries. It enables robotic systems to handle complex fabric shapes and adapt to external force variations, thereby improving production efficiency and quality. As depicted in Fig. 3, this work introduces a coarse-to-fine robotic fabric alignment strategy, which consists of two stages: coarse alignment and fine alignment. In the coarse alignment stage, the system captures the pose of the fabric to be grasped (G-fabric) and the fabric to be aligned (A-fabric). In the fine alignment stage, a carefully designed visual servoing algorithm is employed to align the two fabrics based on visual fabric feature feedback. Additionally, admittance control is applied to ensure stable contact between the fixture and the workspace, enabling reliable fabric grasping and placement.

The following assumptions are made: i) The robot moves the fabric slowly, avoiding shaking, which is common with soft objects during manipulations. ii) The fabric lies within the robot's reachable range. iii) The fabric can be separated from the workspace using specific methods, such as color thresholds. iv) Fabric alignment conducted on the same plane can be transformed into maintaining a separation distance between fabrics. This transformation is referred to as the Manipulation Equivalence of fabric alignment.

IV. ADMITTANCE CONTROL

As the fabric is placed on a rigid workspace, using a hard-contact reaching approach (bypassing the pose directly) may result in collisions between the fixture and the workspace. To address this issue, admittance control is employed to ensure safety between the robot and the workspace while maintaining stable grasping and placement of the fabric. Admittance control operates with pose control as the inner loop and force control as the outer loop, adjusting the robot's motion based on contact forces [19]. A second-order transformation model is used to compute the correction pose \mathbf{x}_c , which is fed into the inner loop to achieve stable pose control. The correction pose is derived as follows:

$$\ddot{\mathbf{x}}_c = \mathbf{A}_m^{-1} (\mathbf{F}_e - \mathbf{A}_b \dot{\mathbf{x}}_e - \mathbf{A}_k \mathbf{x}_e) \quad (1)$$

where $\ddot{\mathbf{x}}_c$ is the desired acceleration. \mathbf{A}_m , \mathbf{A}_b , and \mathbf{A}_k are symmetric positive-definite matrices representing inertia, damping, and stiffness, respectively. \mathbf{F}_e is the difference between the feedback force \mathbf{F} and the desired force \mathbf{F}_d . \mathbf{x}_e represents the difference between the feedback pose \mathbf{x} and the desired pose \mathbf{x}_d .

The Runge-Kutta 4th-order method (RK4) [20] is used to integrate (1) and compute \mathbf{x}_c . The actual pose is then calculated as $\mathbf{x}_{\text{actual}} = \mathbf{x}_c + \mathbf{x}_d$, where \mathbf{x}_d represents the grasping or placement pose, detailed in Sec. V. Fig. 4 provides the block diagram of the admittance control. When the robot comes into contact with the workspace (during grasping or placement), the fixture must securely press against the workspace while maintaining a consistent down-pressure along the z -axis of the force/torque (F/T) sensor to ensure stable contact. The target force is defined as $\mathbf{F}_d = [0, 0, f_z, 0, 0, 0]^T$.

V. FABRIC IDENTIFICATION

A. Fabric Classification

In this work, two fabrics with the same configuration but different areas are used. For simplicity, the fabric area serves as the metric to distinguish between the two fabrics. Fig. 5 illustrates the segmented G-fabric (smaller area) and A-fabric (larger area).

B. Feature Points Detection

By applying *OpenCV/findContours* to the segmented fabrics and performing de-projection from the depth image using known camera intrinsic and extrinsic parameters, the Cartesian contour points in \mathcal{F}_w are obtained as follows:

$$\mathbf{t} = [\mathbf{t}_1, \dots, \mathbf{t}_{n_c}]^T, \quad \mathbf{d} = [\mathbf{d}_1, \dots, \mathbf{d}_{n_c}]^T \quad (2)$$

Here, \mathbf{t} and \mathbf{d} represent the contour points for the G-fabric and A-fabric, respectively, and n_c is the number of contour points. Both \mathbf{t} and \mathbf{d} are ordered, and their respective centers are denoted as $\bar{\mathbf{t}}$ and $\bar{\mathbf{d}}$.

The fabric is asymmetrical, with one side being concave and the other side approximately straight. We define the points along the quasi-straight line as the side points, denoted as \mathbf{t}_s for the G-fabric and \mathbf{d}_s for the A-fabric.

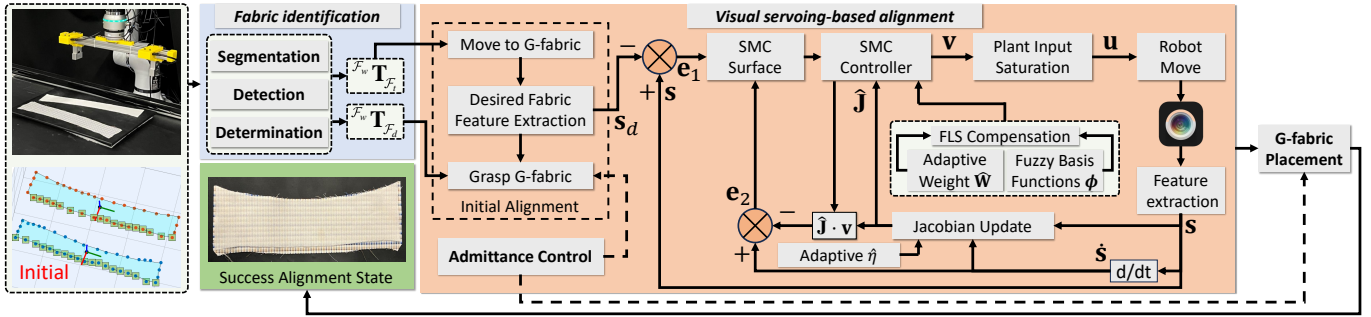


Fig. 3. The structure of the visual servoing-based fabric alignment framework.

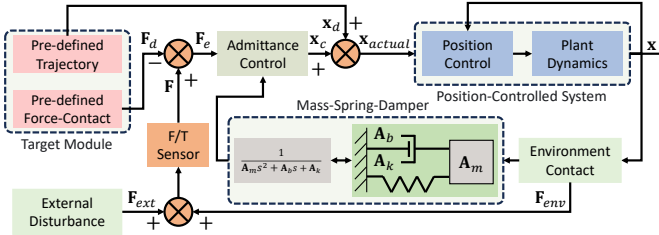


Fig. 4. The block diagram of the admittance control.

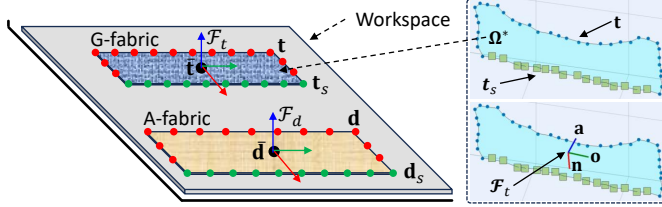


Fig. 5. The visualization of the fabric identification, including fabric segmentation, points detection, and frame determination.

C. Fabric Frame Definition

For simplification, the establishment of the G-fabric frame \mathcal{F}_t and the A-fabric frame \mathcal{F}_d is introduced. Due to the unevenness of the fabric, the A-fabric and G-fabric are not perfectly co-planar. Therefore, an optimal surface covering the fabric must be determined for subsequent grasping and placement. \mathcal{F}_t is used as an example to provide a generalized representation.

The general surface equation is formulated as $h_x x + h_y y + h_z z + h_d = 0$, where $\Omega = [h_x, h_y, h_z, h_d]^\top$ is the hyperparameter. The construction takes the form $\mathbf{f}_i = [\mathbf{t}_i^\top, 1]^\top$, where $i \in [1, n_c]$. Using the distance between \mathbf{t} and the surface defined by the optimal hyperparameter Ω^* , the following cost function is constructed:

$$\Omega^* = \arg \min_{\Omega \in \mathbb{R}^4} \sum_{i=1}^{n_c} \left(\Omega^\top \mathbf{f}_i / \sqrt{h_x^2 + h_y^2 + h_z^2} \right)^2$$

$$\text{s.t. } |\Omega^\top \mathbf{f}_i| / \sqrt{h_x^2 + h_y^2 + h_z^2} \leq \delta_1, \quad i \in [1, n_c] \quad (3)$$

where δ_1 is the distance threshold controlling the fitting accuracy. The function in (3) minimizes the sum of distances between \mathbf{t} and the surface while ensuring that each point-to-surface distance remains below the threshold. The nonlinear solver [21] is applied to (3) to compute Ω^* .

The normal vector of Ω^* is then used as the z -axis of \mathcal{F}_t , defined as $\mathbf{a} = [h_x, h_y, h_z]^\top / \| [h_x, h_y, h_z] \|$. To ensure \mathbf{a} forms an acute angle with the positive z -axis, $\text{dot}(\mathbf{a}, [0, 0, 1])$ is calculated. If the result is negative, \mathbf{a} is reversed. Fig. 5 illustrates the determination of the optimal surface Ω^* .

The direction vector along \mathbf{t}_s is used as the y -axis of \mathcal{F}_t . Principal Component Analysis (PCA) [22] is applied to \mathbf{t}_s to obtain the principal component, which is normalized and used as the y -axis: $\mathbf{o} = \text{PCA}(\mathbf{t}_s)_{\text{main}}$. The x -axis of \mathcal{F}_t is calculated using the right-hand rule as $\mathbf{n} = (\mathbf{o} \times \mathbf{a}) / |\mathbf{o} \times \mathbf{a}|$.

Setting $\bar{\mathbf{t}}$ as the origin \mathbf{p} ensures uniqueness. The transformation matrix from \mathcal{F}_w to \mathcal{F}_t is defined as:

$$\mathcal{F}_w \mathbf{T}_{\mathcal{F}_t} = \begin{bmatrix} \mathbf{n} & \mathbf{o} & \mathbf{a} & \mathbf{p} \\ 0 & 0 & 0 & 1 \end{bmatrix} \quad (4)$$

Finally, repeating the above process for the A-fabric yields $\mathcal{F}_w \mathbf{T}_{\mathcal{F}_d}$. Fig. 5 shows the fabric identification results.

VI. VISUAL SERVOING-BASED FABRIC ALIGNMENT

We define the studied fabric alignment as a classic visual servoing task, focusing on extracting task-specific visual features and tracking their changes. First, the desired fabric feature is introduced, followed by the presentation of the robot-fabric kinematic relationship. Next, a servoing controller is constructed to achieve fabric alignment, and finally, the system's stability is proven, including approximation and control. The end-effector's pose is defined as $\mathbf{r} \in \mathbb{R}^6$, and the velocity command $\mathbf{u} = \dot{\mathbf{r}}$ serves as the control input to be designed.

A. Desired Fabric Feature

As shown in Fig. 2b, the robot moves above the G-fabric using $\mathcal{F}_w \mathbf{T}_{\mathcal{F}_t}$ as defined in (4). At this point, the fixture maintains a fixed distance δ_2 above the G-fabric. Since only the G-fabric is visible in the camera view, the 2D boundary pixels belonging to the G-fabric can be easily extracted using simple image processing algorithms. Subsequently, the 3D boundary points are computed using the camera's intrinsic parameters and are considered the desired fabric feature \mathbf{s}_d . This approach establishes a direct one-to-one correspondence between 2D pixels and 3D points, enhancing robustness against measurement noise [4].

B. Initial Alignment

After extracting \mathbf{s}_d , the fixture descends to grasp the G-fabric. However, due to measurement bias, ${}^{\mathcal{F}_w}\mathbf{T}_{\mathcal{F}_t}$ may not accurately represent the G-fabric's pose. This deviation can cause the fixture to either remain too far from the workspace or apply excessive downward pressure, potentially causing mechanical damage. To address this issue, admittance control is applied to ensure stable grasping while simultaneously avoiding excessive contact between the fixture and the workspace. The robot securely grasps the G-fabric, as shown in Fig. 2c. It then moves above the A-fabric using ${}^{\mathcal{F}_w}\mathbf{T}_{\mathcal{F}_d}$, maintaining the same distance δ_2 as before.

C. Feedback Fabric Feature

After performing the initial alignment, the system transitions into the state shown in Fig. 2d. At this stage, only the two symmetrically positioned eye-in-hand depth cameras are used to observe the workspace during the visual servoing process. First, the 2D boundary pixels from the images captured by the two depth cameras are collected. These pixels belong to the fabric (without distinguishing between the two fabrics at this point). Then, as before, the 3D boundary points Ω are calculated. Next, it is necessary to distinguish Ω into the G-fabric and A-fabric. An intuitive approach would be to use the depth values for classification. However, this can result in inaccuracies because the depth-value range of Ω is typically small. To address this issue, K-means clustering (KMS) [23] is applied for classification, resulting in the G-fabric boundary points Ω_{top} and the A-fabric boundary points Ω_{down} . Finally, Ω_{down} is used as the feedback feature \mathbf{s} .

D. Model Establishment

When the system is in the state shown in Fig. 2d, slight movements of the end-effector cause subtle changes in the fabric feature. The kinematic relationship between \mathbf{s} and \mathbf{r} is defined as the sensorimotor model [24] in the alignment servoing task, expressed as $\mathbf{s} = \mathbf{f}(\mathbf{r})$. Traditionally, an approximate difference equation is directly obtained. However, in this paper, to ensure system stability, several disturbances are considered during the modeling process, followed by compensation design.

Discretization disturbance: Using the Taylor expansion combined with the backward difference formula, the first-order kinematic model is expressed as:

$$\dot{\mathbf{s}} = \frac{\partial \mathbf{f}}{\partial \mathbf{r}} \dot{\mathbf{r}} + \mathbf{d}_s(\mathbf{s}, \mathbf{r}) = \mathbf{J}\mathbf{u} + \mathbf{d}_s(\mathbf{s}, \mathbf{r}) \quad (5)$$

where \mathbf{J} is the kinematic Jacobian matrix (KJM) that transforms robot motions into feature changes, and $\mathbf{d}_s(\mathbf{s}, \mathbf{r})$ is the Taylor expansion remainder. The matrix \mathbf{J} can be regarded as the local motion model of the fabric under quasi-static manipulation by the robot. In practice, it is challenging to compute \mathbf{J} analytically (i.e., $\partial \mathbf{f} / \partial \mathbf{r}$) because the physical properties of the fabric are generally *unknown*. Instead of identifying the full mechanical model, this paper proposes an algorithm to compute local approximations of \mathbf{J} in real time.

Approximation disturbance: As the KJM is estimated online, it is divided into two components: $\mathbf{J} = \hat{\mathbf{J}} + \tilde{\mathbf{J}}$, where

$\hat{\mathbf{J}}$ is the numerical estimation of \mathbf{J} , and $\tilde{\mathbf{J}}$ represents the approximation error. Combining this with (5) gives:

$$\dot{\mathbf{s}} = \hat{\mathbf{J}}\mathbf{u} + \mathbf{d}_J(\tilde{\mathbf{J}}, \mathbf{u}) + \mathbf{d}_s(\mathbf{s}, \mathbf{r}), \quad \mathbf{d}_J(\tilde{\mathbf{J}}, \mathbf{u}) = \tilde{\mathbf{J}}\mathbf{u} \quad (6)$$

where $\mathbf{d}_J(\tilde{\mathbf{J}}, \mathbf{u})$ represents the uncertainty in system modeling caused by the KJM estimation errors.

Saturation Disturbance: In practical scenarios, robots often experience saturation effects, with hard-saturation being the most common [25]. Hard-saturation introduces control discontinuities, which can affect system stability and potentially damage the robot's mechanical structure during operation. Following [26], this paper adopts a smooth saturation model with a continuous form to represent asymmetric saturation nonlinearity, expressed as:

$$u_i(v_i) = u_{i,b} \cdot \text{erf}(v_i \cdot \sqrt{\pi}/2u_{i,b}), \quad i \in [1, 6] \\ u_{i,b} = (\bar{u}_{i,b} + \frac{1}{2}\underline{u}_{i,b}) + (\bar{u}_{i,b} - \frac{1}{2}\underline{u}_{i,b}) \text{sgn}(v_i) \quad (7)$$

where $\mathbf{u} = \mathbf{u}(\mathbf{v})$ represents the saturation effect, and \mathbf{v} is the designed control input. $\bar{u}_{i,b}$ and $\underline{u}_{i,b}$ denote the upper and lower bounds of v_i , respectively. $\text{sgn}(\cdot)$ is the standard sign function, and $\text{erf}(\cdot)$ is the Gaussian error function defined in [26]. When $\bar{u}_{i,b} = \underline{u}_{i,b}$, the saturation model becomes symmetric. The saturation error is defined as $\Delta(\mathbf{v}) = \mathbf{u} - \mathbf{v}$, leading to:

$$\mathbf{u} = \mathbf{v} + \Delta(\mathbf{v}) \quad (8)$$

Total disturbance: Substituting (8) into (6) gives:

$$\dot{\mathbf{s}} = \hat{\mathbf{J}}\mathbf{v} + \underbrace{\mathbf{d}_u(\hat{\mathbf{J}}, \Delta(\mathbf{v})) + \mathbf{d}_J(\tilde{\mathbf{J}}, \mathbf{u}) + \mathbf{d}_s(\mathbf{s}, \mathbf{r})}_{\mathbf{d}(\mathbf{s}, \mathbf{r})} \quad (9)$$

where $\mathbf{d}_u(\hat{\mathbf{J}}, \Delta(\mathbf{v})) = \hat{\mathbf{J}}\Delta(\mathbf{v})$ represents the saturation disturbance, and $\mathbf{d}(\mathbf{s}, \mathbf{r})$ is the total disturbance.

Finally, the system in (9) simplifies to:

$$\dot{\mathbf{s}} = \hat{\mathbf{J}}\mathbf{v} + \mathbf{d}(\mathbf{s}, \mathbf{r}) \quad (10)$$

where \mathbf{v} is the control input to be designed later.

Remark 1. Since we consider regular fabrics, it is reasonable to assume that slight $\dot{\mathbf{r}}$ will produce slight $\dot{\mathbf{s}}$. As the Cartesian points obtained from the camera model are used as visual features, a one-to-one mapping relationship $\mathbf{s} = \mathbf{f}(\mathbf{r})$ is assumed to hold locally.

E. Fuzzy Approximation

To enhance system stability, the fuzzy logic system (FLS) [27] is introduced to model the nonlinear disturbance $\mathbf{d}(\mathbf{s}, \mathbf{r})$ and compensate for it within the system. This results in:

$$\mathbf{d}(\mathbf{s}, \mathbf{r}) = \mathbf{W}^\top \phi + \varepsilon \quad (11)$$

where \mathbf{W} is the ideal constant weight matrix, and ϕ is the pre-defined fuzzy basis vector [27]. The matrix \mathbf{W} is unknown and requires online estimation. Let $\hat{\mathbf{W}}$ denote the numerical estimate of \mathbf{W} , and $\tilde{\mathbf{W}} = \mathbf{W} - \hat{\mathbf{W}}$ represent the estimation error. FLS is used to estimate the total disturbance and compensate for it within the controller.

Lemma 1. [27] For any $x \in \mathbb{R}$ and any $\kappa > 0$, it is certain that: $0 \leq |x| - x \tanh(x/\kappa) \leq 0.2785\kappa$.

Lemma 2. [27] For any continuous vector $\mathbf{f}(\mathbf{x})$ defined on the compact set Ω , and for any constant vector $\varepsilon > 0$, the FLS satisfies the following property:

$$\sup_{\mathbf{x} \in \Omega} \|\mathbf{f}(\mathbf{x}) - \mathbf{W}^\top \phi(\mathbf{x})\| \leq \|\varepsilon\| \quad (12)$$

Assumptions 1. There exists an ideal weight matrix \mathbf{W} such that $\|\varepsilon\|^2 \leq \eta$, where $\eta > 0$ is a constant for all $\mathbf{x} \in \Omega$.

F. Controller Design

Sliding mode control (SMC) is introduced to achieve closed-loop alignment. Two tracking errors are defined as:

$$\mathbf{e}_1 = \mathbf{s} - \mathbf{s}_d, \quad \mathbf{e}_2 = \dot{\mathbf{s}} - \hat{\mathbf{J}}\mathbf{v} \quad (13)$$

where \mathbf{e}_1 represents the alignment error and \mathbf{e}_2 represents the model estimation error. Here, \mathbf{s}_d is the desired fabric feature defined in Sec. VI-A. Notably, \mathbf{s}_d can be time-varying, representing an improvement over methods that assume it to be constant [28]. Through (13), SMC integrates model estimation and controller design while providing a unified stability analysis.

By computing the time derivative of (13), we obtain:

$$\dot{\mathbf{e}}_1 = \dot{\mathbf{s}} - \dot{\mathbf{s}}_d, \quad \dot{\mathbf{e}}_2 = \ddot{\mathbf{s}} - \dot{\hat{\mathbf{J}}}\mathbf{v} - \hat{\mathbf{J}}\dot{\mathbf{v}} \quad (14)$$

The sliding mode surfaces are constructed as:

$$\sigma_1 = \mathbf{K}_1 \mathbf{e}_1 + \dot{\mathbf{e}}_1, \quad \sigma_2 = \mathbf{K}_2 \mathbf{e}_2 + \dot{\mathbf{e}}_2 \quad (15)$$

where \mathbf{K}_1 and \mathbf{K}_2 are symmetric positive-definite constant matrices that regulate the convergence speed of σ_1 and σ_2 . Ensuring the convergence of σ_1 guarantees the convergence of \mathbf{e}_1 , meaning \mathbf{s} approaches \mathbf{s}_d . This completes the fabric alignment task. Theoretically, SMC-based control systems offer superior robustness compared to conventional feedback control systems [4]. Using (15) and (14), the time derivative of σ_1 is given by:

$$\dot{\sigma}_1 = \mathbf{K}_1(\hat{\mathbf{J}}\mathbf{v} + \mathbf{W}^\top \phi + \varepsilon - \dot{\mathbf{s}}_d) + \ddot{\mathbf{e}}_1 \quad (16)$$

The velocity controller is designed as:

$$\begin{aligned} \mathbf{v} &= \hat{\mathbf{J}}^+ \mathbf{K}_1^{-1}(-\sigma_1 + \mathbf{K}_1 \dot{\mathbf{s}}_d - \ddot{\mathbf{e}}_1 - \mathbf{K}_1 \hat{\mathbf{W}}^\top \phi) \\ \dot{\mathbf{W}} &= \Gamma(\phi \sigma_1^\top \mathbf{K}_1 - \beta \hat{\mathbf{W}}) \end{aligned} \quad (17)$$

where $\hat{\mathbf{J}}^+$ is the pseudo-inverse of $\hat{\mathbf{J}}$, $\Gamma > 0$ is the coefficient matrix, and β is a small positive constant. Since the design avoids power terms and the sign function, \mathbf{v} remains continuous, preventing chattering. To ensure system convergence, the quadratic function is defined as $V_1(\sigma_1) = \frac{1}{2} \sigma_1^\top \sigma_1$. By computing the time derivative of V_1 and using (16) and (17), we have:

$$\dot{V}_1(\sigma_1) = -\sigma_1^\top \sigma_1 + \sigma_1^\top \mathbf{K}_1 \varepsilon + \sigma_1^\top \mathbf{K}_1 \tilde{\mathbf{W}}^\top \phi \quad (18)$$

Referencing Assumption 1 and applying Young's inequality, the following relation is obtained:

$$\sigma_1^\top \mathbf{K}_1 \varepsilon \leq \frac{1}{4} \lambda_{\mathbf{K}_1}^2 \|\sigma_1\|^2 + \eta \quad (19)$$

where $\lambda_{\mathbf{K}_1}$ denotes the maximum eigenvalue of \mathbf{K}_1 . Substituting (19) into (18), we have:

$$\dot{V}_1(\sigma_1) \leq -(1 - \frac{1}{4} \lambda_{\mathbf{K}_1}^2) \|\sigma_1\|^2 + \sigma_1^\top \mathbf{K}_1 \tilde{\mathbf{W}}^\top \phi + \eta \quad (20)$$

The KJM is adaptively computed as:

$$\dot{\mathbf{J}} = (\ddot{\mathbf{s}} - \hat{\mathbf{J}}\dot{\mathbf{v}} - \mathbf{K}_2^{-1} \varpi) \mathbf{v}^+ \quad (21)$$

$$\varpi = -\sigma_2 - \ddot{\mathbf{e}}_2 - \sigma_2^\top \tanh(\frac{1}{\gamma_1}) \hat{\eta}, \quad \dot{\hat{\eta}} = \tanh(\frac{1}{\gamma_1}) - \gamma_2 \hat{\eta}$$

where γ_1 and γ_2 are positive constants. The term $\ddot{\mathbf{s}} - \hat{\mathbf{J}}\dot{\mathbf{v}}$ reflects the updates of \mathbf{s} and \mathbf{v} with respect to $\hat{\mathbf{J}}$. The term ϖ compensates for system modeling errors, thereby improving stability. The parameter $\hat{\eta}$ compensates for the FLS approximation error, and the estimation error is given by $\tilde{\eta} = \eta - \hat{\eta}$.

The adaptive rule $\dot{\hat{\eta}}$ employs the δ -modification algorithm [29] to address parameter drift caused by estimation errors. It is important to note that this rule does not guarantee identification of the true value of \mathbf{J} . Instead, its objective is to compute a numerical solution for \mathbf{J} that continuously satisfies the system model (10).

Similarly, the quadratic function for σ_2 is defined as: $V_2(\sigma_2) = \frac{1}{2} \sigma_2^\top \sigma_2$. Using (21), the time-derivative of V_2 yields:

$$\dot{V}_2(\sigma_2) = -\sigma_2^\top \sigma_2 - \tanh(1/\gamma_1) \hat{\eta} \quad (22)$$

G. Stability Analysis

Proposition 1. Consider the closed-loop system (10) under Assumption 1, with the velocity controller (17), the model estimator (21), and the adaptive rule $\dot{\hat{\eta}}$. Given the desired fabric feature \mathbf{s}_d , there exists an appropriate set of control parameters that ensure: (i) all signals remain uniformly ultimately bounded (UUB), and (ii) the alignment error \mathbf{e}_1 asymptotically converges to a compact set around zero.

proof: Consider the following quadratic function:

$$V = V_1(\sigma_1) + \frac{\text{tr}(\tilde{\mathbf{W}}^\top \Gamma^{-1} \tilde{\mathbf{W}})}{2} + V_2(\sigma_2) + \frac{\tilde{\eta}^2}{2} \quad (23)$$

Computing the time-derivative of (23), we obtain:

$$\dot{V} = \sigma_1^\top \dot{\sigma}_1 - \text{tr}(\tilde{\mathbf{W}}^\top \Gamma^{-1} \dot{\tilde{\mathbf{W}}}) + \sigma_2^\top \dot{\sigma}_2 - \tilde{\eta} \dot{\hat{\eta}} \quad (24)$$

Using Young's inequality, the following relations are derived:

$$\begin{aligned} \gamma_2 \tilde{\eta} \dot{\hat{\eta}} &\leq -\frac{\gamma_2}{2} \tilde{\eta}^2 + \frac{\gamma_2}{2} \eta^2 \\ \text{tr}(\tilde{\mathbf{W}}^\top \beta \hat{\mathbf{W}}) &\leq -\frac{\beta}{2} \|\tilde{\mathbf{W}}\|^2 + \frac{\beta}{2} \|\mathbf{W}\|^2 \end{aligned} \quad (25)$$

Taking into account (18), (22), (25), the adaptive rules for $\dot{\hat{\eta}}$ and $\hat{\mathbf{W}}$, and Lemma 1, we have:

$$\dot{V} \leq -aV + b \quad (26)$$

where $a = \min(2 - \lambda_{\mathbf{K}_1}^2/2, 2, \beta, \gamma_2)$, and the residual term is $b = \beta \|\mathbf{W}\|^2/2 + \gamma_2 \eta^2/2 + 0.2785 \gamma_1 \eta > 0$. By selecting an appropriate value for \mathbf{K}_1 to ensure $a > 0$, the states σ_1 , σ_2 , \mathbf{W} , and $\tilde{\eta}$ exhibit asymptotic convergence and remain UUB. This result guarantees that \mathbf{e}_1 will eventually converge to a

compact set near zero. Furthermore, it demonstrates that the estimation error $\hat{\mathbf{J}}$ is bounded. ■

The SMC employed is a type of overdetermined controller, meaning \mathbf{e}_1 can only converge to a local range determined by the feasibility of \mathbf{s}_d . In visual servoing, the local minimization problem based on the Jacobian formulation is inevitable [4]. Algorithm 1 outlines the proposed fabric alignment framework. The parameter $\delta_3 > 0$ regulates the alignment accuracy.

Algorithm 1 Fabric alignment process

Require:

- 1: Fabric identification in Sec. V $\leftarrow \mathcal{F}_w \mathbf{T}_{\mathcal{F}_t}$ and $\mathcal{F}_w \mathbf{T}_{\mathcal{F}_d}$
- 2: The robot moves to $\mathcal{F}_w \mathbf{T}_{\mathcal{F}_t}$
- 3: Calculate the desired fabric feature \mathbf{s}_d
- 4: Grasp the G-fabric + Admittance control: $\mathbf{x}_d \leftarrow \mathcal{F}_w \mathbf{T}_{\mathcal{F}_t}$
- 5: The robot moves the G-fabric to $\mathcal{F}_w \mathbf{T}_{\mathcal{F}_d}$
- 6: The robot conducts tiny movements to initialize $\hat{\mathbf{J}}(0)$
- 7: Start the visual servoing
- 8: **while** $\|\mathbf{e}_1\| \geq \delta_3$ **do**
- 9: Record the current robot pose \mathbf{r} and velocity \mathbf{u}
- 10: Record the current fabric feature \mathbf{s}
- 11: Calculate the error signals \mathbf{e}_1 and $\mathbf{e}_2 \leftarrow (13)$
- 12: Calculate the surfaces σ_1 and $\sigma_2 \leftarrow (15)$
- 13: Update the FLS weight $\hat{\mathbf{W}} \leftarrow (17)$
- 14: Update the velocity command $\mathbf{v} \leftarrow (17)$
- 15: Update the KJM $\hat{\mathbf{J}} \leftarrow (21)$
- 16: Update the plant input $\mathbf{u} \leftarrow (7)$
- 17: The robot moves using the updated \mathbf{u}
- 18: **end while**
- 19: Place the G-fabric + Admittance control: $\mathbf{x}_d \leftarrow \mathcal{F}_w \mathbf{T}_{\mathcal{F}_d}$
- 20: Fabric alignment is completed

VII. EXPERIMENTAL RESULTS

A. Platform Setup

To validate the proposed fabric alignment system, we designed a flowchart, as shown in Fig. 6, to execute the task and collect statistical data for the experimental results. Fig. 7 illustrates the experimental setup for validating the fabric alignment tasks. A RealSense RGB-D calibrated D455 camera is used to observe the initial alignment from a top-down perspective, following an eye-to-hand configuration. The HansRobot (Model: E05) is employed as the robotic platform, as shown in Fig. 7a. A KWR75B 6-DOF F/T sensor is used to detect the contact force between the robot and the environment, enabling admittance control. A zero-offset calibration was conducted to ensure accurate measurements, as shown in Fig. 7b. The setup combines a 3030 aluminum profile with 3D-printed fabric fixtures installed at the end of the F/T sensor. Two pneumatic needle-type suction cups (Model: WJT20*45) are used as fabric grippers. These suction cups are attached to the aluminum profile via 3D-printed connectors and are horizontally positioned at both ends of the profile, as shown in Fig. 7e. A high-pressure air hose (6 bar) from the laboratory's built-in system is connected to a program-controlled solenoid valve, which is managed by the computer, as shown in Fig. 7c and Fig. 7d. Two RealSense RGB-D

D405 cameras are horizontally mounted at both ends of the aluminum profile using 3D-printed connectors, following an eye-in-hand configuration. Both D405 cameras provide visual feedback without requiring extrinsic calibration. To ensure a comprehensive evaluation, two scenarios are considered: flat placement and tilted placement. Each scenario includes two fabric positioning configurations. Fig. 7f - Fig. 7i depict the four cases.

To meet the assumptions outlined in Sec. III, the saturation limit for 3-DOF translation is set to 0.03 m/s, while for 3-DOF rotation, it is set to 10°/s. The proposed algorithm is implemented in Ubuntu 20.04 using the ROS1/Python API interface. Image processing, alignment control, and admittance control operate within a servo-control loop running at 28 Hz.

B. Validation of Admittance Control

In this section, we evaluate the admittance control introduced in Sec. IV. Admittance control is applied during the grasping and placing of the G-fabric. For simplicity, we focus on fabric grasping. Four cases, shown in Fig. 7 (Cases 1–4), are used. Each grasping scenario is repeated fifty times to calculate the success rate, with two conditions being tested: with and without admittance control. The target contact force is set as $\mathbf{F}_d = [0, 0, -2.16, 0, 0, 0]$, where $-2.16N$ represents the desired contact force along the z -axis of the F/T sensor.

Fig. 8 presents the grasping results. The grasping pose is determined using (4). The results show that admittance control significantly improves the success rate (highlighted in red). Although it is possible to manually adjust the end-effector's pose to regulate the downward force, such adjustments are open-loop in nature and can easily result in mechanical actuator failures or damage to the workspace. Fig. 9 illustrates the F/T profiles for Case 1. The red line represents the F/T feedback, while the blue line indicates the desired signal. Since admittance control activates when the fixture contacts the workspace, the blue line is presented intermittently. The admittance control starts at 1.69 s and ends at 1.97 s.

The tracking curves clearly demonstrate that admittance control effectively maintains stable contact forces and torques. For the 3-DOF force, static contact is achieved along the xy -axes, while constant pressure is quickly established along the z -axis. For the 3-DOF torque, although the curves deviate visibly from the desired values, this is due to the small units on the vertical axis. Despite these deviations, the zero rotational energy of the 3-DOF torque is effectively maintained.

C. Validation of Fabric Identification

Fig. 10a shows the segmentation results of two differently sized fabrics in various positions. The striped fabric represents the A-fabric, while the white textured fabric represents the G-fabric. The results demonstrate that distinguishing fabric types based on the area metric is effective across different positions.

Fig. 10b illustrates the detection of contour points (t and d), center points (\bar{t} and \bar{d}), and side points (t_s and d_s). The RGB image from the D455 camera is converted into a binary image using mask processing. Farthest Point Sampling (FPS) [30] is applied to extract a fixed set of contour pixels. Subsequently, the 3D contour points are computed by mapping

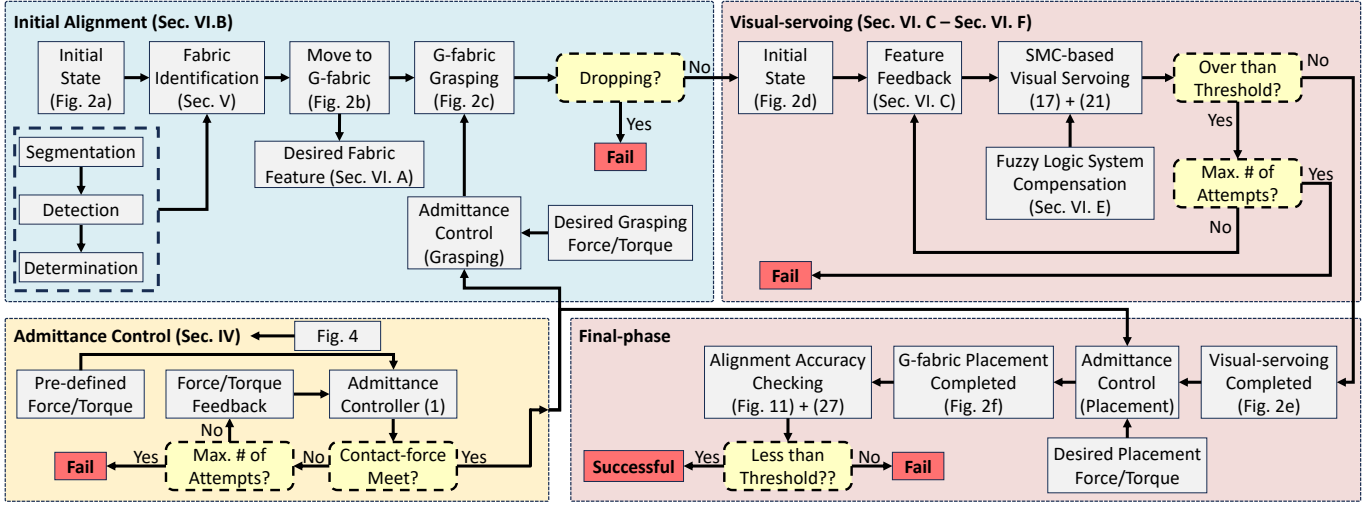


Fig. 6. Flowchart of the autonomous fabric alignment framework.

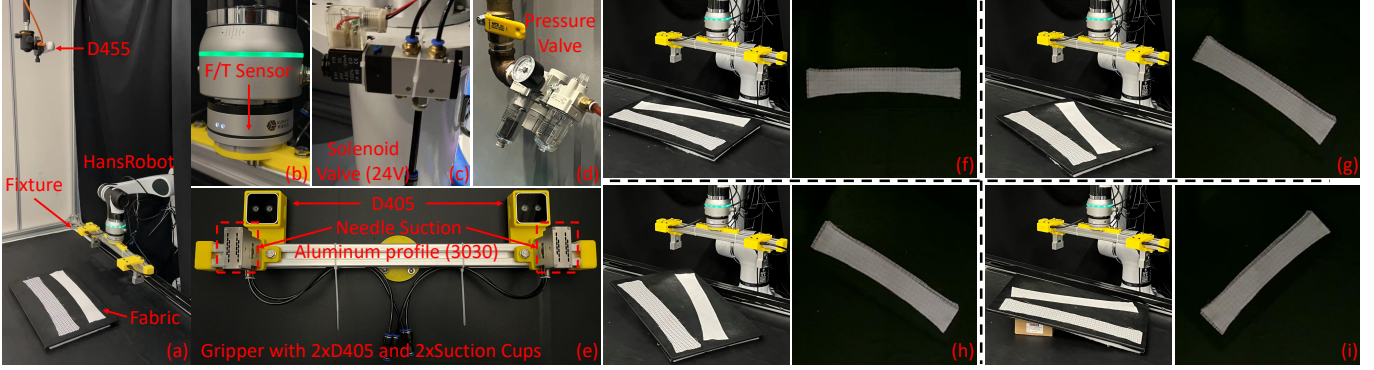


Fig. 7. (a)-(e): experimental setup; (f) - (i): the alignment of fabrics in four placement configurations, where the left subplots show the initial states and the right subplots show the final aligned states.

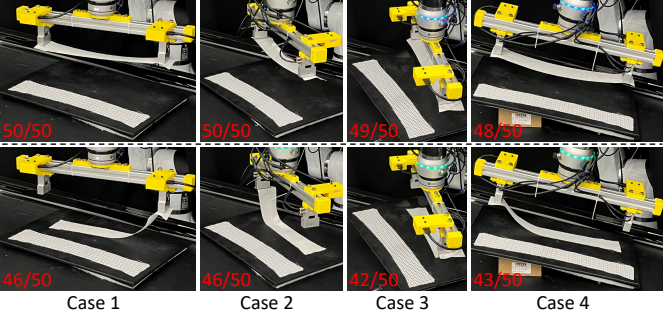


Fig. 8. The fabric grasping with (first row) and without (second row) admittance control in four placement configurations shown in Fig. 7.

the corresponding 2D pixels using the intrinsic and extrinsic camera parameters. The results show that the contour points are evenly arranged, effectively representing the boundary information, and the detection of side points is precise.

Fig. 10b also depicts the fabric frames (\mathcal{F}_t and \mathcal{F}_d). The light blue region represents the optimal co-planar surface of the fabric contour points (t or d), determined using (3), which is used to establish the z-axis of the fabric frame. Notably, the z-axis of the fabric frame forms an acute angle with the z-axis of \mathcal{F}_w . The y-axis of the fabric frame is constrained to be

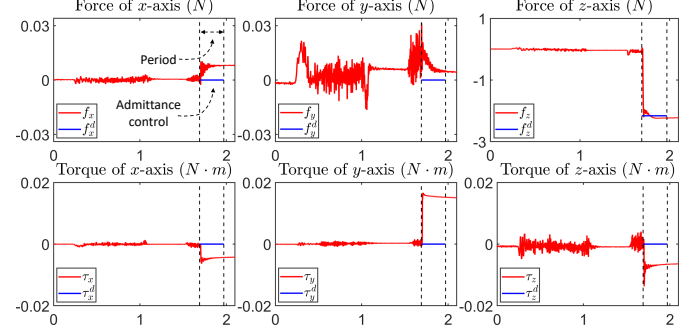


Fig. 9. The F/T profiles of Case 1. The abscissa is the time, unit is s.

horizontally oriented to the right along the fabric surface. The results confirm that (4) accurately establishes the directional fabric frame, significantly aiding subsequent grasping and placement tasks.

D. Alignment Metric Construction

Three metrics are used to evaluate alignment performance: success rate, runtime, and alignment accuracy. The runtime and alignment accuracy are calculated only for successful cases. The runtime is measured in seconds (s), while alignment

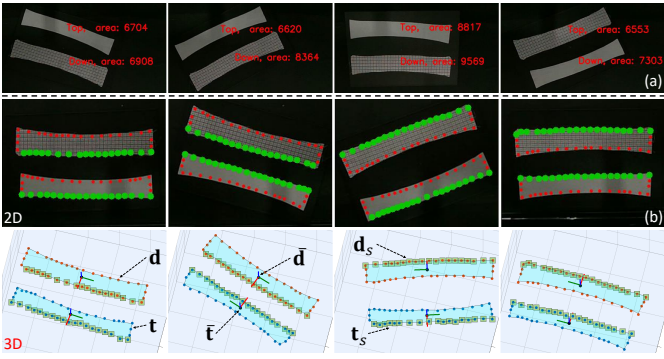


Fig. 10. Validations of fabric identification, including type segmentation, points detection, and frame determination.

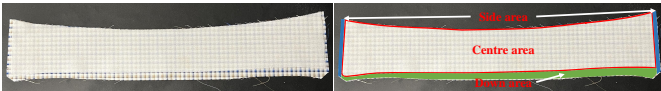


Fig. 11. Visualization of the alignment accuracy calculation.

accuracy is a dimensionless variable. Alignment accuracy is determined by capturing the alignment results with a high-precision camera and manually calculating the measurements. Fig. 11 illustrates the calculation process for alignment accuracy. The two blue regions on the left and right represent the side areas where the A-fabric extends beyond the G-fabric in the horizontal direction. These areas are denoted as ρ_1 and ρ_2 . The lower area represents the vertical region where the A-fabric exceeds the G-fabric, denoted as ρ_3 . The alignment accuracy is calculated as:

$$\text{Accuracy} = \|\left[\max(\rho_1, \rho_2)/\min(\rho_1, \rho_2), \rho_3/\rho_3^*\right]\| \quad (27)$$

where ρ_3^* is measured offline.

E. Same Shape-size Fabric Alignment

The experimental scenarios utilize the four placement configurations depicted in Fig. 7. Due to space constraints, only the scenarios shown in Fig. 7g and Fig. 7i are presented. Four methods are employed for a comprehensive performance comparison in each scenario, as illustrated in Table I. Admittance control is not applied in (a), meaning a hard-contact approach is used for grasping and placement. Method (d) activates all modules. To verify system robustness, three types of disturbances are introduced: (i) Random noise added to the D455, indirectly affecting the establishment of the fabric frame. (ii) Random noise added to the F/T sensor to evaluate admittance control. (iii) Random movement of the base plate

during the visual-servoing process. Fig. 12 and Fig. 13 present the fabric alignment results. The first row shows the initial alignment, captured by a handheld camera from a third-person perspective. The last three rows depict the visual-servoing-based alignment, captured from two D405 cameras and a handheld camera. The red arrow indicates the G-fabric's movement direction. The results demonstrate that the proposed control framework effectively accomplishes fabric alignment. The fabric grasping remains stable without any dropping during movement, and the placement yields satisfactory results. This highlights the beneficial role of admittance control in fabric grasping and placement.

The results also confirm the accuracy of the fabric frame (4). Even under slope conditions, the G-fabric remains parallel to the A-fabric while maintaining a certain distance. This demonstrates the effectiveness of the proposed fabric frame determination. After the initial alignment, the system achieves near-predetermined alignment criteria, with minimal deviations when moving above the A-fabric. A relatively accurate initial alignment facilitates subsequent visual-servoing-based alignment, accelerating the overall alignment process. After visual-servoing adjustments, the fabrics are well aligned. Finally, by reactivating admittance control, the G-fabric is stably placed above the A-fabric. Adjusting the threshold value δ_3 allows fine-tuning of alignment accuracy.

Table II compares three metrics—success rate, runtime, and alignment accuracy—across four placement positions and the four approaches outlined in Table I. Method (d) achieves the highest success rate, with (c) performing significantly better than (b) and (a). The primary reasons for failure are unsuccessful grasping of the G-fabric and dropping during the visual-servoing process. This emphasizes the importance of admittance control in ensuring stable contact between the fabric and the fixture.

In terms of runtime, (a) is the fastest, while (d) is the slowest. The times for (b) and (c) are similar. The faster runtime of (a) is due to the absence of FLS compensation and admittance control, while (d) activates both modules. Regarding alignment accuracy, (d) achieves the highest precision, followed by (c), with (b) slightly outperforming (a). This indicates that FLS and admittance control significantly improve alignment accuracy. Although the experimental setup is stable, utilizing regular fabrics and lacking significant external disturbances, the compensation effect of FLS is not highly pronounced. However, FLS remains beneficial for dynamic and rapid alignments.

F. Different Shape-size Fabric Alignment

This section verifies the framework's generalization, focusing on alignment performance with different fabric shapes and configurations. To achieve this, three additional fabric shapes were cut based on the original fabric, as shown in Fig. 14. These four fabrics are commonly used in the stacking processes of collars and cuffs in clothing production. Fabric (1) represents the original shape, while fabrics (2)–(4) are newly added. Validation is performed using approach (d) from Table I.

Due to space constraints, only the final manipulation results are shown in Fig. 14. The left side of each subplot represents

TABLE I
DESCRIPTIONS OF FOUR COMPARISON APPROACHES IN THE FABRIC ALIGNMENT VALIDATION. YES MEANS USED, AND NO MEANS UNUSED.

	SMC	FLS	Admittance Control
(a)	Yes	No	No
(b)	Yes	Yes	No
(c)	Yes	No	Yes
(d)	Yes	Yes	Yes

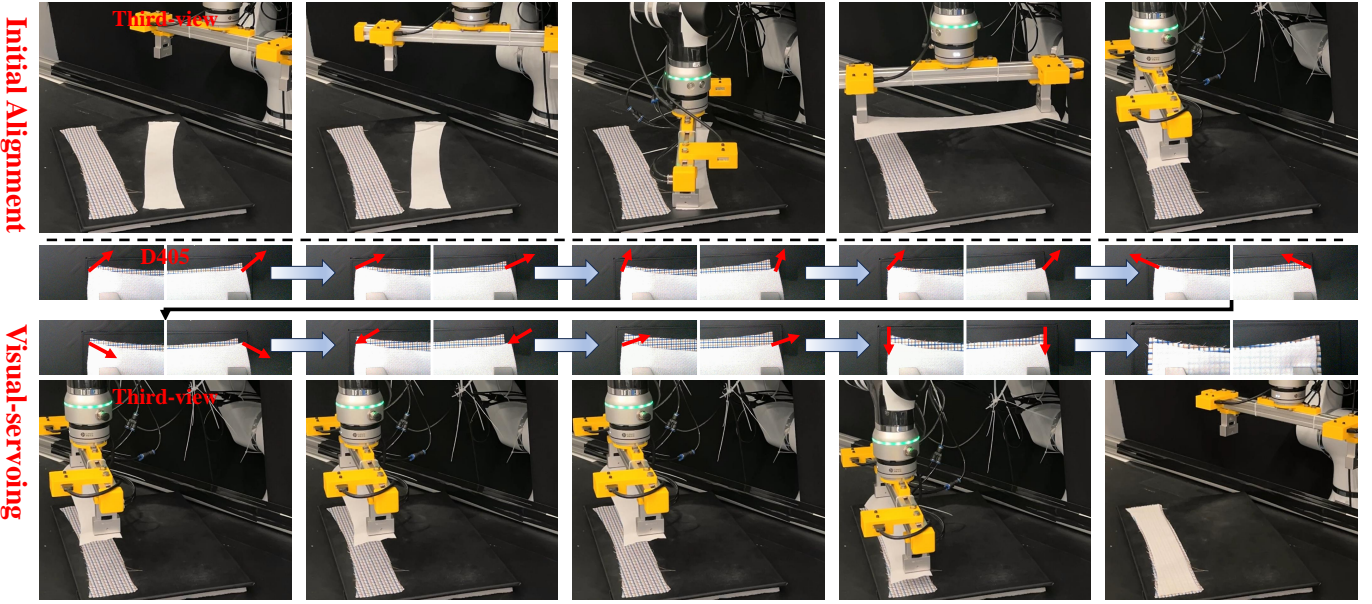


Fig. 12. Overall validations of the proposed fabric alignment framework, adopting the case shown in Fig. 7g.

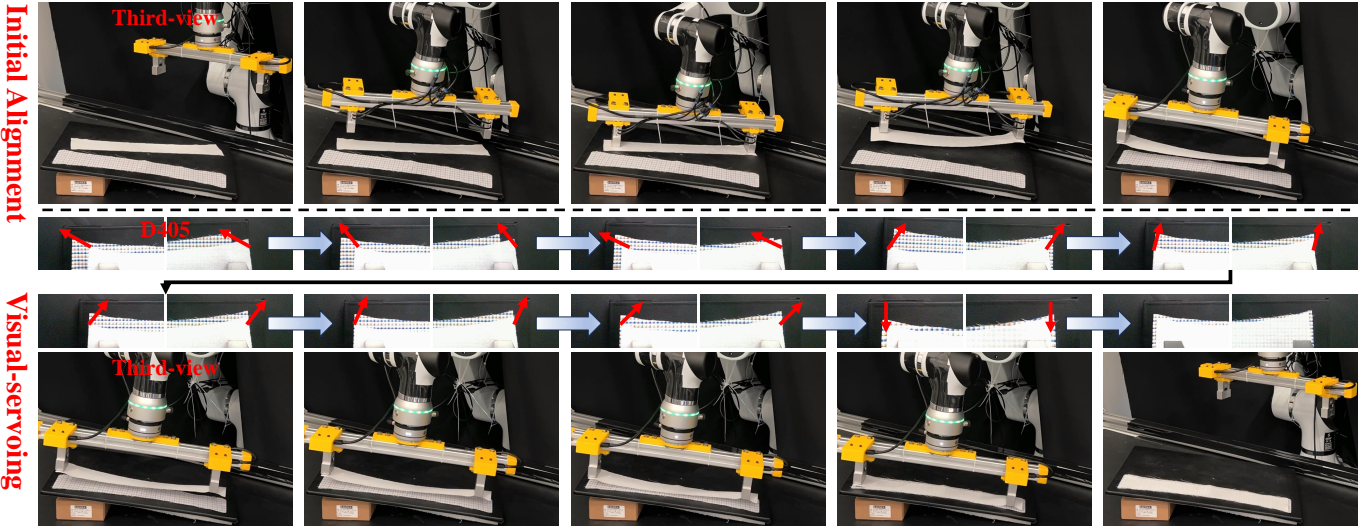


Fig. 13. Overall validations of the proposed fabric alignment framework, adopting the case shown in Fig. 7i.

TABLE II
COMPARISON VERIFICATION RESULTS OF THREE PERFORMANCE INDICATORS UNDER FOUR PLACEMENT CONFIGURATIONS SHOWN IN FIG. 7 AND FOUR COMPARATIVE APPROACHES ILLUSTRATED IN TABLE I.

Case 1			Case 2			Case 3			Case 4		
Success rate	Running time	Alignment Accuracy	Success rate	Running time	Alignment Accuracy	Success rate	Running time	Alignment Accuracy	Success rate	Running time	Alignment Accuracy
(a) 16/20	21.5 ± 0.91	2.14 ± 0.51	15/20	21.6 ± 0.84	2.23 ± 0.62	14/20	23.3 ± 0.98	2.47 ± 0.58	15/20	23.2 ± 0.81	2.45 ± 0.52
(b) 16/20	22.5 ± 0.82	2.06 ± 0.36	16/20	22.4 ± 0.81	2.13 ± 0.42	15/20	24.8 ± 1.32	2.21 ± 0.33	16/20	24.5 ± 1.03	2.24 ± 0.13
(c) 19/20	24.3 ± 0.97	1.92 ± 0.24	19/20	24.5 ± 0.78	1.93 ± 0.32	19/20	26.8 ± 1.18	1.89 ± 0.28	19/20	26.8 ± 0.97	1.85 ± 0.23
(d) 20/20	25.4 ± 0.91	1.48 ± 0.06	20/20	25.4 ± 0.87	1.49 ± 0.08	20/20	27.5 ± 1.02	1.56 ± 0.12	20/20	27.3 ± 1.13	1.52 ± 0.11

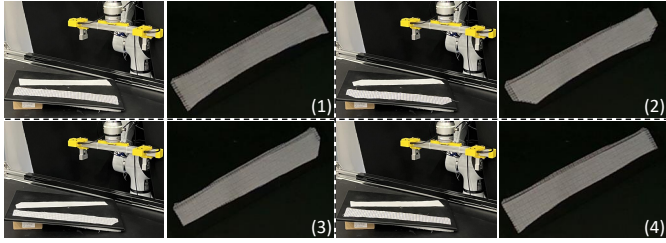


Fig. 14. Alignment results for four different fabric shapes and configurations.

TABLE III
COMPARATIVE RESULTS OF MANIPULATION PERFORMANCE UNDER FOUR DIFFERENT TYPES OF FABRICS.

	Success Rate	Running time (s)	Alignment Accuracy
(1)	20/20	27.3 ± 1.13	1.52 ± 0.11
(2)	17/20	31.8 ± 2.21	1.78 ± 0.89
(3)	19/20	29.6 ± 1.89	1.67 ± 0.47
(4)	20/20	28.7 ± 1.27	1.61 ± 0.58

the initial state, while the right side shows the final aligned state. Table III provides a performance comparison for the four different fabrics. The results demonstrate that the proposed alignment framework performs effectively across the four fabric shapes. However, there is a slight decrease in performance when manipulating fabric (2). This is likely due to the limited length available for grasping fabric (2), as the suction cup's position on the fixture is fixed.

These results confirm the effectiveness of the proposed coarse-to-fine fabric alignment framework and highlight the importance of admittance control in maintaining stable fabric contact. By incorporating dynamic, online adaptive compensation based on FLS to address system disturbances, alignment accuracy is further improved. Additionally, the integration of visual servoing enables the proposed approach to adapt to the most commonly used fabric shapes. By designing specific fabric features, the system's generalization capability can be enhanced.

Most fabric alignment devices rely on an open-loop approach, essentially a “point-and-shoot” method. This places significant demands on system model accuracy, increasing development complexity. In contrast, the proposed framework does not require a precise system model or symmetric grasping. As long as the fixture can securely grasp the fabric, the system can achieve alignment through visual servoing adjustments. The innovation of this paper lies in the introduction of a visual servoing-based adjustment strategy, enabling various fabric alignment tasks to be accomplished by modifying the visual features used.

VIII. CONCLUSIONS

The article presents a visual servoing-based fabric alignment framework for unstructured environments, addressing discretization, approximation, and saturation disturbances. Firstly, an optimization-based directed fabric frame is constructed to enable subsequent alignment servoing. Secondly, an SMC-based controller is proposed to integrate identification and control, while an FLS-based compensator is designed to handle system disturbances. Thirdly, admittance control is

implemented to maintain stable contact between the gripper and the fabric. Finally, a Lyapunov stability proof is provided, demonstrating the boundedness of signals in the closed-loop system and the convergence of alignment errors. However, the framework has some limitations. For instance, the suction cup positions are fixed, making it difficult to adapt to various fabric types. Additionally, a calibrated depth camera is required, which may be challenging to implement in practical environments. Future work will focus on designing a fully model-free control scheme that does not rely on calibration or pre-measured fabric characteristics.

REFERENCES

- [1] B. Kehoe, S. Patil, P. Abbeel, and K. Goldberg, “A survey of research on cloud robotics and automation,” *IEEE Transactions on automation science and engineering*, vol. 12, no. 2, pp. 398–409, 2015.
- [2] J. Parker, R. Dubey, F. Paul, and R. Becker, “Robotic fabric handling for automating garment manufacturing,” 1983.
- [3] H. A. Kadi and K. Terzić, “Data-driven robotic manipulation of cloth-like deformable objects: The present, challenges and future prospects,” *Sensors*, vol. 23, no. 5, p. 2389, 2023.
- [4] J. Qi, G. Ma, J. Zhu, P. Zhou, Y. Lyu, H. Zhang, and D. Navarro-Alarcon, “Contour moments based manipulation of composite rigid-deformable objects with finite time model estimation and shape/position control,” *IEEE/ASME Transactions on Mechatronics*, 2021.
- [5] P. Zhou, P. Zheng, J. Qi, C. Li, H.-Y. Lee, Y. Pan, C. Yang, D. Navarro-Alarcon, and J. Pan, “Bimanual deformable bag manipulation using a structure-of-interest based neural dynamics model,” *IEEE/ASME Transactions on Mechatronics*, 2024.
- [6] Z. Hu, T. Han, P. Sun, J. Pan, and D. Manocha, “3-d deformable object manipulation using deep neural networks,” *IEEE Robotics and Automation Letters*, vol. 4, no. 4, pp. 4255–4261, 2019.
- [7] S. Donaire, J. Borras, G. Alenya, and C. Torras, “A versatile gripper for cloth manipulation,” *IEEE Robotics and Automation Letters*, vol. 5, no. 4, pp. 6520–6527, 2020.
- [8] D. Hinwood, D. Herath, and R. Goecke, “Towards the design of a human-inspired gripper for textile manipulation,” in *2020 IEEE 16th International Conference on Automation Science and Engineering (CASE)*. IEEE, 2020, pp. 913–920.
- [9] T. Kim and Y.-L. Park, “Robotic platform for automatic alignment and placement of fabric patterns for smart manufacturing in garment industry,” *International Journal of Precision Engineering and Manufacturing*, vol. 24, no. 9, pp. 1549–1561, 2023.
- [10] D. Kragic, H. I. Christensen, *et al.*, “Survey on visual servoing for manipulation,” *Computational Vision and Active Perception Laboratory, Fiskartorpsv*, vol. 15, p. 2002, 2002.
- [11] D. Navarro-Alarcon, Y.-H. Liu, J. G. Romero, and P. Li, “Model-free visually servoed deformation control of elastic objects by robot manipulators,” *IEEE Transactions on Robotics*, vol. 29, no. 6, pp. 1457–1468, 2013.
- [12] D. Navarro-Alarcon, Y.-H. Liu, J. G. Romero, and P. Li, “On the visual deformation servoing of compliant objects: Uncalibrated control methods and experiments,” *The International Journal of Robotics Research*, vol. 33, no. 11, pp. 1462–1480, 2014.
- [13] D. Andronas, E. Kampourakis, K. Bakopoulos, C. Gkournelos, P. Angelakis, and S. Makris, “Model-based robot control for human-robot flexible material co-manipulation,” in *2021 26th IEEE International Conference on Emerging Technologies and Factory Automation (ETFA)*. IEEE, 2021, pp. 1–8.
- [14] G. Nicola, S. Mutti, E. Villagrossi, and N. Pedrocchi, “Depth image-based deformation estimation of deformable objects for collaborative mobile transportation,” in *2023 32nd IEEE International Conference on Robot and Human Interactive Communication (RO-MAN)*. IEEE, 2023, pp. 2658–2664.
- [15] S. D’Avella, A. M. Sundaram, W. Friedl, P. Tripicchio, and M. A. Roa, “Multimodal grasp planner for hybrid grippers in cluttered scenes,” *IEEE Robotics and Automation Letters*, vol. 8, no. 4, pp. 2030–2037, 2023.
- [16] K. P. Tee, R. Yan, and H. Li, “Adaptive admittance control of a robot manipulator under task space constraint,” in *2010 IEEE International Conference on Robotics and Automation*. IEEE, 2010, pp. 5181–5186.
- [17] Z. Li, B. Huang, Z. Ye, M. Deng, and C. Yang, “Physical human-robot interaction of a robotic exoskeleton by admittance control,” *IEEE Transactions on Industrial Electronics*, vol. 65, no. 12, pp. 9614–9624, 2018.

- [18] W. He, C. Xue, X. Yu, Z. Li, and C. Yang, "Admittance-based controller design for physical human–robot interaction in the constrained task space," *IEEE Transactions on Automation Science and Engineering*, vol. 17, no. 4, pp. 1937–1949, 2020.
- [19] A. Q. Keemink, H. Van der Kooij, and A. H. Stienen, "Admittance control for physical human–robot interaction," *The International Journal of Robotics Research*, vol. 37, no. 11, pp. 1421–1444, 2018.
- [20] J. H. Cartwright and O. Piro, "The dynamics of runge–kutta methods," *International Journal of Bifurcation and Chaos*, vol. 2, no. 03, pp. 427–449, 1992.
- [21] J. A. Andersson, J. Gillis, G. Horn, J. B. Rawlings, and M. Diehl, "Casadi: a software framework for nonlinear optimization and optimal control," *Mathematical Programming Computation*, vol. 11, pp. 1–36, 2019.
- [22] H. Abdi and L. J. Williams, "Principal component analysis," *Wiley interdisciplinary reviews: computational statistics*, vol. 2, no. 4, pp. 433–459, 2010.
- [23] K. Krishna and M. N. Murty, "Genetic k-means algorithm," *IEEE Transactions on Systems, Man, and Cybernetics, Part B (Cybernetics)*, vol. 29, no. 3, pp. 433–439, 1999.
- [24] J. Qi, W. Ma, D. Navarro-Alarcon, H. Gao, and G. Ma, "Adaptive shape servoing of elastic rods using parameterized regression features and auto-tuning motion controls," *arXiv preprint arXiv:2008.06896*, 2020.
- [25] X. Shao, P. Pustina, M. Stölzle, G. Sun, A. De Luca, L. Wu, and C. Della Santina, "Model-based control for soft robots with system uncertainties and input saturation," *IEEE Transactions on Industrial Electronics*, 2023.
- [26] J. Ma, S. S. Ge, Z. Zheng, and D. Hu, "Adaptive nn control of a class of nonlinear systems with asymmetric saturation actuators," *IEEE transactions on neural networks and learning systems*, vol. 26, no. 7, pp. 1532–1538, 2014.
- [27] Q. Zhou, L. Wang, C. Wu, H. Li, and H. Du, "Adaptive fuzzy control for nonstrict-feedback systems with input saturation and output constraint," *IEEE Transactions on Systems, Man, and Cybernetics: Systems*, vol. 47, no. 1, pp. 1–12, 2016.
- [28] Lagneau, K. Romain, M. Alexandre, and Maud, "Automatic shape control of deformable wires based on model-free visual servoing," *IEEE Robotics and Automation Letters*, vol. 5, no. 4, pp. 5252–5259, 2020.
- [29] P. A. Ioannou and J. Sun, *Robust adaptive control*. Courier Corporation, 2012.
- [30] J. Qi, G. Ma, P. Zhou, H. Zhang, Y. Lyu, and D. Navarro-Alarcon, "Towards latent space based manipulation of elastic rods using autoencoder models and robust centerline extractions," *Advanced Robotics*, vol. 36, no. 3, pp. 101–115, 2022.